

Galaxy cluster mass profiles

L. M. Voigt[★] and A. C. Fabian

Institute of Astronomy, Madingley Road, Cambridge CB3 0HA

Accepted 2006 February 3. Received 2006 January 31; in original form 2005 June 13

ABSTRACT

Accurate measurements of the mass distribution in galaxy and cluster haloes are essential to test the cold dark matter (CDM) paradigm. The cosmological model predicts a universal shape for the density profile in all haloes, independent of halo mass. Its profile has a ‘cuspy’ centre, with no evidence for the constant density core. In this paper, we carry out a careful analysis of 12 galaxy clusters, using *Chandra* data to compute the mass distribution in each system under the assumption of hydrostatic equilibrium. Due to their low concentration, clusters provide ideal objects for studying the central cusps in dark matter haloes. The majority of the systems are consistent with the CDM model, but four objects exhibit flat inner density profiles. We suggest that the flat inner profile found for these clusters is due to an underestimation of the mass in the cluster centre (rather than any problem with the CDM model), since these objects also have a centrally peaked gas mass fraction. We discuss possible causes for erroneously low-mass measurements in the cores of some systems.

Key words: galaxies: clusters: general – dark matter – X-rays: galaxies.

1 INTRODUCTION

In hierarchical collapse models, N -body simulations predict a universal shape for the mass distribution in dark matter haloes from dwarf galaxies ($10^7 M_\odot$) to massive clusters ($10^{15} M_\odot$), independent of the value of the cosmological parameters. The density profile differs strongly from a simple single power law, predicted in early theoretical work (Gunn & Gott 1972; Fillmore & Goldreich 1984; Hoffman & Shaham 1985; White & Zaritsky 1992), and is centrally concentrated with an inner cusp $\rho(r) \propto r^{-\alpha}$. The universality of the structure of dark matter haloes formed through hierarchical clustering was ‘discovered’ in simulations performed by Navarro, Frenk & White (1995, 1996, 1997), hereafter NFW.¹ In these early studies, an inner slope with $\alpha = 1.0$ provided the best fit to the spherically averaged density profiles. This was supported by various authors (Cole & Lacey 1996; Kravtsov, Klypin & Khokhlov 1997; Tormen, Bouchet & White 1997). Later simulations at higher resolution indicated a steeper central cusp, with $\alpha = 1.5$ (Fukushige & Makino 1997, 2001, 2003; Moore et al. 1999; Ghigna et al. 2000; Klypin et al. 2001). A density profile similar to the NFW profile, but with $\alpha = 1.5$ was suggested by Moore et al. (1999), hereafter M99.

A thorough understanding of the predictions made by simulations is essential in order to test the cold dark matter (CDM) paradigm against observations. There are several issues which need to be

addressed by simulators, in particular in the high-density central regions of haloes where large numbers of particles and fine time-resolution are required. In recent work, there has been some debate over the form of the profile at the innermost resolved radii ($r < 0.01 r_{\text{vir}}$). Power et al. (2003), Hayashi et al. (2004) and Navarro et al. (2004) suggested that the inner density profile does not converge to a well-defined power law, but continues to flatten inwards. Diemand et al. (2005), on the other hand, disputed this result, continuing to support the existence of a central asymptotic power law to the density profiles.

A further issue which remains unresolved numerically is the universality of the core profile. Jing & Suto (2000), for example, found that the inner slope steepens with decreasing halo mass. In addition, using analytical arguments, Hoffman & Shaham (1985) and Syer & White (1998) showed that the halo profile should depend on the power spectrum of initial density fluctuations, with an inner slope given by $3(n+3)/(n+4)$ and $3(n+3)/(n+5)$, respectively, where n is the power-law index of the spectrum.

Nevertheless, there are two robust predictions made by simulations which may be tested against observations: the density profile in CDM haloes differs strongly from a single power law, and the inner region is cuspy with a power-law slope in the range $1.0 \lesssim \alpha \lesssim 1.5$ down to at least 1 per cent of the virial radius. In this paper, we obtain mass profiles under the assumptions of hydrostatic equilibrium and spherical symmetry for a sample of X-ray-peaked galaxy clusters using *Chandra* data. Straightforward deprojection techniques are robust and work well on such clusters. In addition, clusters haloes have smaller concentrations than galaxies, making them ideal objects to study cusps. Work on the inner density slope of clusters of galaxies has also been carried out in recent studies

[★]E-mail: lisa.voigt@yahoo.com

¹ Simulations by NFW built on earlier, pioneering works by Frenk et al. (1988), Dubinski & Carlberg (1991) and Crone, Evrard & Richstone (1994), which identified the absence of a constant density core in dark matter haloes.

Table 1. Summary of the *Chandra* observations. Cluster redshift, observation date, exposure time, good time interval, X-ray emission peak, luminosity distance and angular scale. Both observations available for RXJ 1347.5–1145 were used.

Cluster	Redshift	Observation date	Exposure time (ks)	GTI (ks)	Emission peak (J2000) RA	Dec.	D_L (Mpc)	D_A (kpc arcsec $^{-1}$)
Abell 3112	0.0750	2001 September 15	17.1	13.5	03 17 57.7	−44 14 16.9	335.2	1.4
2A 0335+096	0.0347	2000 September 06	20.0	18.1	03 38 40.6	+09 58 11.0	140.6	0.7
Abell 478	0.0880	2001 January 27	42.9	38.9	04 13 25.2	+10 27 53.9	396.9	1.6
PKS 0745–191	0.1028	2001 June 16	17.9	14.6	07 47 31.2	−19 17 38.8	468.5	1.9
RXJ 1347.5–1145(1)	0.4510	2000 March 5	9.1	8.0	13 47 30.5	−11 45 09.5	2492.9	5.7
RXJ 1347.5–1145(2)	0.4510	2000 April 29	10.1	7.2	13 47 30.5	−11 45 09.5	2492.9	5.7
Abell 1795	0.0632	2000 March 21	19.7	15.6	13 48 52.5	+26 35 37.8	280.0	1.2
Abell 1835	0.2523	1999 December 11	19.8	18.9	14 01 01.9	+02 52 43.4	1262.4	3.9
Abell 3581	0.0218	2001 June 07	7.3	6.0	14 07 29.8	−27 01 04.2	93.6	0.4
Abell 2029	0.0767	2000 April 12	19.9	19.8	15 10 56.1	+05 44 40.6	343.2	1.1
RXJ 1532.9+3021	0.3615	2001 August 26	9.5	6.2	15 32 53.8	+30 20 58.5	1916.3	5.0
MS 2137.3–2353	0.3130	1999 November 18	44.2	19.5	21 40 15.2	−23 39 39.9	1618.8	4.7
Sersic 159–03 (AS 1101)	0.0564	2001 August 13	10.1	9.8	23 13 58.3	−42 43 35.0	248.7	1.1

by Katayama & Hayashida (2004), Arabadjis, Bautz & Arabadjis (2004) and Pointecouteau, Arnaud & Pratt (2005).

A Λ CDM cosmology with $\Omega_\Lambda = 0.7$ and $h = 0.7$ is adopted.

2 CLUSTER SAMPLE

The cluster sample used is listed in Table 1. Observations of objects with known short central cooling times, indicating a relatively relaxed object, were obtained from the *Chandra* archive.² The sample of 12 objects was chosen to cover a range in cluster redshift ($z = 0.02$ – 0.46) and intracluster medium (ICM) temperature ($k_B T = 2$ – 15 keV). High-redshift clusters observed by *Chandra* tend to be hotter, and in this sense the sample is not statistically complete; however, this will not in general affect the analyses carried out, and any biases introduced by the limited sample are discussed where relevant.

Data processing was carried out using the CIAO (*Chandra* Interactive Analysis of Observations) software package available from the *Chandra* X-ray Centre (CXC). Level 2 events files were updated to include the latest calibration. Only those X-ray events with ASCA grade classifications 0, 2, 3, 4 and 6 were included in the cleaned data set. Further screening was carried out to remove time intervals contaminated by background flares. The light curves were analysed using the script LC_CLEAN written by M. Markevitch and provided by the CXC. The observation length remaining after screening (GTI; good time interval) is listed for each object in Table 1.

3 SPECTRAL ANALYSIS

3.1 Extracting spectra

For the spectral analysis, each cluster was divided into circular annuli around the X-ray emission peak, with strong point sources identified by eye and masked out. Regions disturbed by, for example, merging subclusters and radio lobes, were also removed (see Section 3.4). A spectrum was extracted for each annulus using the CIAO DMEXTRACT tool. The spectra were binned to contain at least 20 counts per PHA channel to enable the use of chi-square statistics.

² Observations using the ACIS-S3 detector only were used.

Ancillary-response and response matrices were constructed using the CIAO MKWARF and MKRMF programs.

3.2 The spectral model

Spectra were fit in the 0.5–7.0 keV energy range using the XSPEC (Arnaud 1996) software package. The emission from each shell was modelled using the MEKAL (Mewe, Gronenschild & van den Oord 1985) plasma emission code, incorporating the Fe L calculations of Liedahl, Osterheld & Goldstein (1995), and absorbed by the PHABS (Balucinska-Church & McCammon 1992) photoelectric absorption code to take into account galactic absorption along the line of sight. The emission was deprojected using the PROJECT model provided in XSPEC.

The free parameters in the model were the temperature, metallicity and emission measure. The elements were assumed to be present in the solar ratios measured by Anders & Grevesse (1989) and the abundance allowed to vary between shells. The Galactic absorption column density was left as a free parameter in the fits,³ although linked between shells. The nominal (measured by Dickey & Lockman 1990) and best-fitting N_H values are shown in Table 2, together with the minimum chi-square of the fit.

3.3 Deprojection

A series of tests have been carried out by Johnstone et al. (2005) to check that PROJECT produces the correct results when applied to known synthetic data. With the exception of the outermost shell, the temperature and density profiles obtained with PROJECT match very well with the synthetic input profiles.

An apparent increase in density in the outermost shell results from the assumption of zero-emission exterior to that region. Clearly,

³ The low-energy quantum efficiency of the ACIS chips has been continuously degraded since launch. Tools have been provided by the CXC to account for the loss in effective area, although whether or not the correction is applied has a negligible effect on the temperature and emission integral profiles when the Galactic absorption column density is left as a free parameter in the fits. With the correction applied, the best-fitting N_H is often much less than the nominal value, suggesting that the tools tend to ‘over-correct’ the data. Following the work of Voigt & Fabian (2004) and Birzan et al. (2004), we use uncorrected data in order to avoid best-fitting galactic absorption measurements consistent with zero.

Table 2. Best-fitting absorption column density, N_{H} , chi-square and reduced chi-square for the model. The nominal galactic absorption column along the line of sight to the cluster from Dickey & Lockman (1990) is also tabulated.

Cluster	Fitted N_{H} (10^{20} cm^{-2})	Galactic N_{H} (10^{20} cm^{-2})	χ^2 (d.o.f.)	χ^2_{ν}
Abell 3112	$5.42^{+0.22}_{-0.22}$	1.95	1482 (1388)	1.07
2A 0335+096	$27.23^{+0.18}_{-0.18}$	17.8	2682 (1968)	1.36
Abell 478	$33.46^{+0.16}_{-0.16}$	15.2	4243 (3458)	1.23
PKS 0745–191	$42.77^{+0.35}_{-0.34}$	42.4	2486 (2251)	1.10
RXJ 1347.5–1145	$5.18^{+0.72}_{-0.41}$	4.85	805 (859)	0.94
Abell 1795	$1.82^{+0.13}_{-0.13}$	1.19	2110 (1861)	1.13
Abell 1835	$2.78^{+0.24}_{-0.24}$	2.32	1551 (1445)	1.07
Abell 3581	$9.87^{+0.53}_{-0.50}$	4.52	716 (653)	1.10
Abell 2029	$4.14^{+0.12}_{-0.11}$	3.05	2878 (2555)	1.13
RXJ 1532.9+3021	$6.14^{+0.68}_{-0.65}$	2.16	403 (379)	1.06
MS 2137.3–2353	$4.63^{+0.44}_{-0.45}$	3.55	596 (541)	1.10
Sersic 159–03	$6.07^{+0.39}_{-0.39}$	1.79	917 (844)	1.09

there will be some counts attributed to this shell which were emitted at larger radii and the emission integral will be overestimated. This effect will be seen out to large radii – even if the cluster counts exterior to the outer region are negligible, the background emission will contribute to the emission integral – although will become less significant as the virial radius is approached.

We note that the measured gas temperature in the penultimate annulus is slightly higher when the outer shell is removed from the fit, although consistent within the 1σ limits. The temperature in the outer annulus will be slightly overestimated if the temperature rises exterior to this region and underestimated if it falls.

3.4 Masked regions

To obtain an accurate measure of the cluster mass distribution, we are interested in the ambient gas properties. For the spectral analyses, the following features were therefore masked out from the images: a shock front in 2A 0335+096 spanning a sector between 150° and 210° , 50–60 arcsec from the cluster centre; radio lobes in Abell 478; the south-east quadrant in RXJ 1347.5–1145 containing a bright subclump and the bright filament extending southwards from the core in Abell 1795.

3.5 Spectral fits

The reduced chi-squares of the fits obtained using the spectral model described in Section 3.2 are less than ~ 1.1 for the majority of objects in the sample (see Table 2), showing that the X-ray emission is well described by a single-phase plasma at each radius. We note that the reduced chi-square is greatest for the fits to 2A 0335+096 and Abell 478.

4 TEMPERATURE, DENSITY AND PRESSURE PROFILES

Gas temperature, density and pressure profiles are shown for a representative sample of clusters in Fig. 1.

4.1 Temperature and density

The temperature distribution is obtained directly from the spectral fits and the density profile from the normalization of the MEKAL spectrum, $K = EI/[4 \times 10^{14} \pi D_A^2 (1+z)^2]$, where $EI (= \int n_e n_H dV)$ is the emission integral. The electron number density at the centre of each shell is estimated as $\langle n_e \rangle = (1.2EI/V)^{1/2}$, where we have used the relation $n_e \approx 1.2n_H$ and V is the volume of the shell.

4.2 Pressure

At the high temperatures and low densities in the ICM, the appropriate pressure equation of state is the ideal gas law, given by $P = nk_B T$, where $n \approx 1.92n_e$ is the number of particles per unit volume. The electron pressure, P_e , at the mid-point of each shell is computed by multiplying the electron density by the temperature. The uncertainties in n_e and T are added in quadrature to find the uncertainty in P_e (i.e. the density and temperature are assumed to be independent). We note that contour plots of shell normalization against temperature are approximately circular, showing the assumption is a reasonable one).

5 MASS MEASUREMENTS

5.1 Total mass

Determining masses using X-ray data allows the cluster mass to be computed as a function of radius. The gas is assumed to be in hydrostatic equilibrium within the cluster potential. The equation of hydrostatic equilibrium for a spherically symmetric system is given by

$$M_{\text{tot}}(<r_j) = -\frac{1}{G} \frac{r_j^2}{\rho_{\text{gas},j}} \left(\frac{dP}{dr} \right)_j, \quad (1)$$

where P is the thermal pressure.

5.1.1 Calculation

The total mass enclosed within radius r_j is calculated from equation (1), where r_j is the radial distance from the centre of the cluster to the mid-point between two consecutive shells. The pressure gradient at the mid-point is estimated as

$$\left(\frac{dP}{dr} \right)_j = \frac{P_{i+1} - P_i}{r_{i+1} - r_i}, \quad (2)$$

where P_i is the pressure at the centre of the i th shell, r_i is the radial distance to the centre of the i th shell and $r_j = (r_i + r_{i+1})/2$. The gas density at r_j is calculated using linear interpolation, such that

$$\rho_{\text{gas}}(r_j) = \frac{\rho_{\text{gas}}(r_{i+1}) + \rho_{\text{gas}}(r_i)}{2}, \quad (3)$$

where $\rho_{\text{gas},i}$, the gas density at the centre of the i th shell, is found from the electron number density using the relation $\rho_{\text{gas},i} = \mu m_H n_{\text{gas},i} \approx 1.92 \mu m_H n_{e,i}$. The uncertainties are calculated using a Monte Carlo technique whereby both the pressure and density data are perturbed 1000 times. PKS 0745–191 does not exhibit a smooth pressure profile in the centre and so measurements made using equation (2) do not produce a monotonically increasing mass profile. We compute the mass profile in the inner region of this object by binning together the first and second and the third and fourth data points in the pressure and gas density profiles.

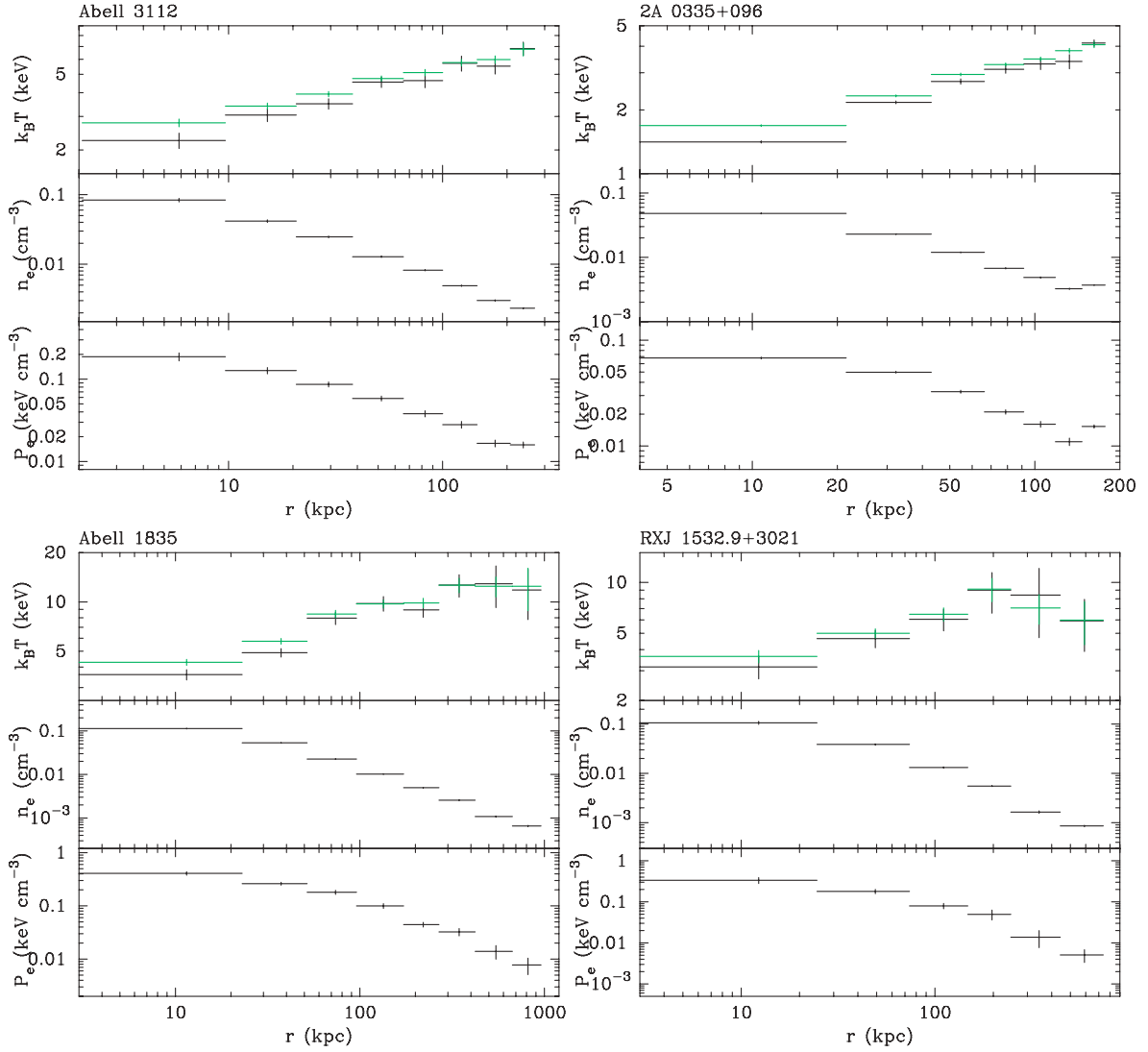


Figure 1. Deprojected gas temperature, density and pressure profiles for a representative sample of clusters. Projected gas temperature profiles are shown in green.

Computing the mass profile involves determining the pressure gradient at the mid-point between the centres of consecutive shells. By estimating the gradient using equation (2), we effectively fit a straight line between adjacent data points. (The accuracy of the method may therefore be improved by increasing the number of data points.) Neighbouring mass points may be slightly correlated, but data points further away than one will not be correlated with one another. Several authors fit a parametric model to the temperature and gas density profiles and use this to compute the mass profile. The data points in this case are not independent and finding the best-fitting model to the mass profile using chi-square statistics will be statistically invalid. The method used here, made possible due to the high spatial resolution of the *Chandra* Observatory, therefore provides an improvement over previous analyses.

The mass profiles are shown for the sample in Fig. 2. The outer-mass data point is removed in all but three clusters (RXJ 1347.5–1145, RXJ 1532.9+3021 and MS 2137.3–2353). This is because the artificially high gas density and pressure in the outer

bin⁴ cause the outer-mass data point to be significantly underestimated in the majority of objects. For the high-redshift systems ($z \gtrsim 0.3$), the outer-mass data point is estimated to be accurate to within a few per cent. The accuracy of the outer data point is assessed by calculating the mass profile from the data obtained both with and without the outer shell included in the spectral analysis. As an example, the mass profiles obtained for Abell 1795 and RXJ 1347.5–1145 are shown in Fig. 3. The percentage decrease in the mass measured in the penultimate shell is less than 1 per cent for RXJ 1347.5–1145 and about 50 per cent for Abell 1795 when the outer annulus is not included in the spectral fit.

Removing the outer-mass data point in clusters such as Abell 1795 before analysing the mass profile is vital. Current structure formation models predict that the mass profile should ‘turn-over’ at some characteristic radius. If an erroneously low-mass data point is included in the outer region then this will

⁴ See Section 3.3.

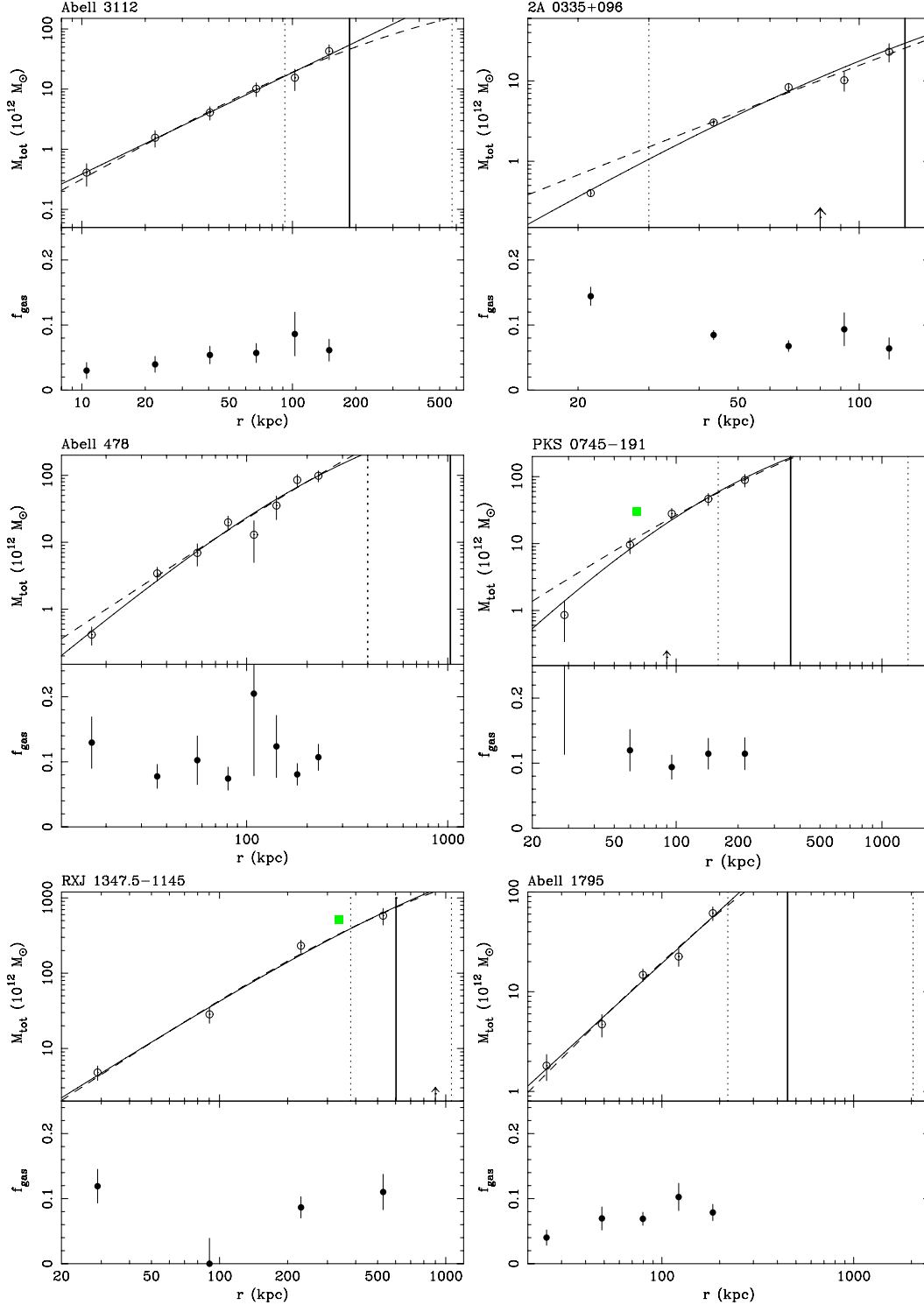


Figure 2. Total (dark plus baryonic) mass profiles (upper) and gas mass fraction profiles (lower). The error bars show the 1σ uncertainties in the measurements. The solid line shows the best-fitting M_2F_1 model to the data, with α a free parameter in the fit. The dashed line shows the best-fitting NFW model ($\alpha = 1$) to the data. For the latter model, the inner 30 kpc is removed from the fit to the profiles of 2A 0335+096, Abell 478, PKS 0745-191 and Seric 159-03 (see text). The best-fitting scale radius and 1σ limits, obtained with $\alpha = 1$, are shown by solid and dotted vertical lines, respectively. The arrow indicates the best-fitting scale radius for the M_2F_1 model. (In the cases where an arrow is not shown the best-fitting model tends to a power law.) Lensing masses taken from Allen (1998) are indicated (green filled squares).

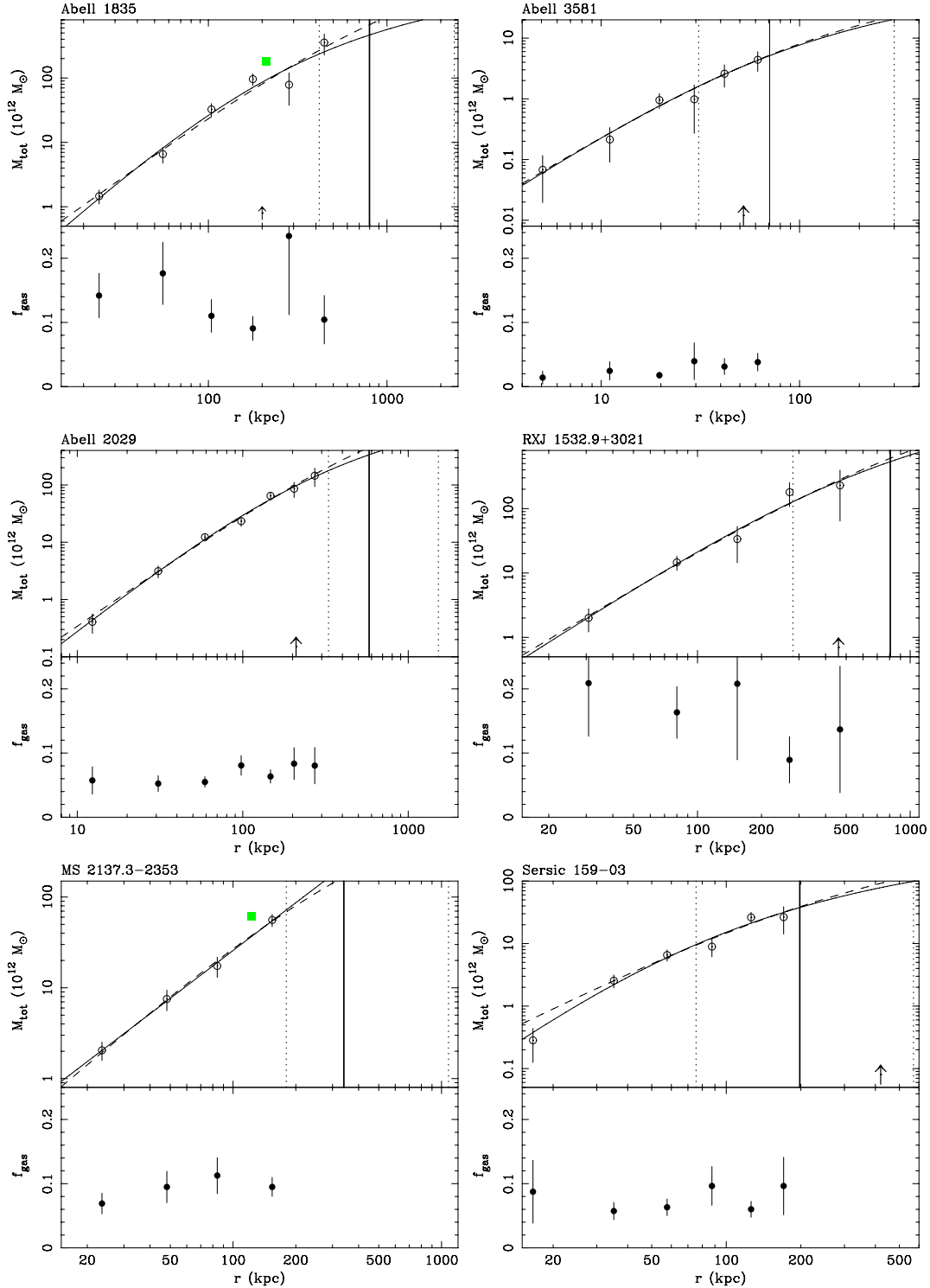


Figure 2 – continued

wrongly indicate that the profile is curving away from a power law.

5.1.2 Lensing masses

Mass measurements from strong lensing analyses are also plotted in Fig. 2 for PKS 0745–191, RXJ 1347.4–1145, Abell 1835 and

MS 2137.3–2353 (Allen 1998). In each case, the lensing mass is larger than the X-ray mass by a factor of between 1.5 and 3. This discrepancy is also found by Allen (1998), if a single-phase spectral model (i.e. no cooling flow) is adopted. It is difficult at this stage to draw any strong conclusions about the difference in the measurements. The lensing results are quoted without uncertainties and there are several difficulties with this method, such as adopting the

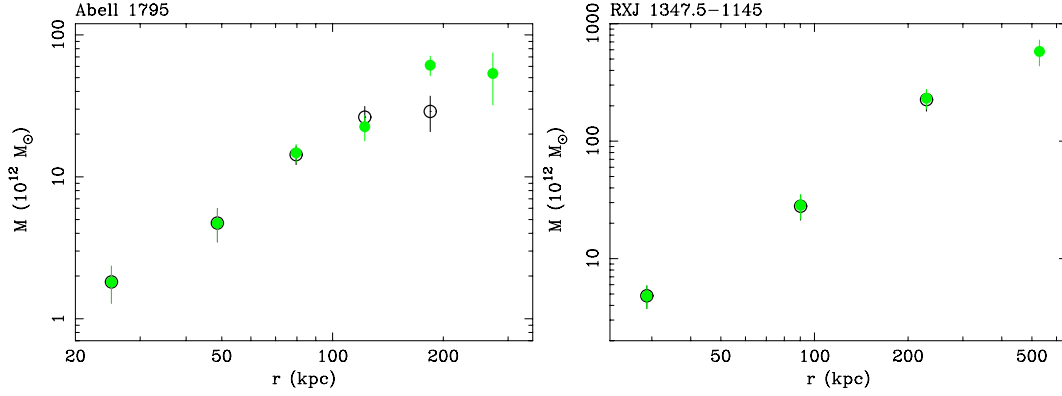


Figure 3. Mass profiles computed using data from spectral fits obtained with (green filled circles) and without (black open circles) the outer shell included.

correct geometry, obtaining accurate arc redshifts and the unknown presence of secondary matter along the line of sight (Wambsganss, Bode & Ostriker 2005). Similarly, the masses obtained from the X-ray analysis are also dependent on several assumptions, including the spectral and geometrical models adopted. It will be important in future work to improve on both methods until an agreement is reached.

5.2 Gas mass and gas mass fraction

The integrated gas mass profile is calculated using the sum

$$M_{\text{gas}}(< r_k) = \sum_{i=1}^n \frac{4}{3} \pi (r_k^3 - r_{k-1}^3) \rho_{\text{gas}}(r_i), \quad (4)$$

where r_k is the radial distance to the outer boundary of the i th shell.

The gas mass fraction is the ratio of the total gas mass to the total gravitating mass within a fixed volume

$$f_{\text{gas}} = \frac{M_{\text{gas}}(< r_j)}{M_{\text{tot}}(< r_j)}. \quad (5)$$

The total gas mass within r_j is computed from the gas mass profiles using linear interpolation. The gas mass fraction profiles are plotted in Fig. 2.

We note that the total integrated mass within a particular volume, calculated from the equation of hydrostatic equilibrium, is dependent upon the pressure gradient and gas density at that radius only, and is completely unaffected by the regions interior (or exterior) to that radius. For the gas mass profile, on the other hand, the integrated mass is calculated by summing from the centre outwards and any error in the measurement at small radii will propagate out to larger radii. However, the gas mass at small radii is much less than at large radii and any uncertainty in the measurements in the core are unlikely to have a significant effect on the gas mass profile further out.

6 DARK MATTER PROFILES FROM SIMULATIONS

The generalized equation for the density distribution in dark matter haloes, including all models with a ‘cuspy’ core, is given by

$$\rho(x) = \frac{\rho_0}{x^\alpha (1 + x^\gamma)^{(\beta-\alpha)/\gamma}}, \quad (6)$$

where $x = r/r_s$. The scale radius, r_s , is a free parameter. The indices (α, β, γ) for the NFW and M99 models are (1.0, 3.0, 1.0) and (1.5,

3.0, 1.5), respectively. A simple analytic model for the mass is easily obtained for each of these special cases, with

$$M(< x) = \begin{cases} 4\pi\rho_0 r_s^3 \left[\ln(1+x) - \frac{x}{1+x} \right] & \text{for NFW} \\ \frac{8}{3}\pi\rho_0 r_s^3 \ln(1+x^{3/2}) & \text{for M99.} \end{cases} \quad (7)$$

A generalized mass profile, valid for any values of the indices, may be written

$$M(< x) = 4\pi\rho_0 r_s^3 \frac{x^{\alpha_3} {}_2F_1 \left[\alpha_3/\gamma, (\beta-\alpha)/\gamma; (\alpha_3+\gamma)/\gamma; -x^\gamma \right]}{\alpha_3}, \quad (8)$$

where $\alpha_3 = 3 - \alpha$. The hypergeometric function ${}_2F_1$ may be evaluated numerically. We refer to this model as M_2F_1 .

6.1 Definition of concentration

The mass enclosed within a region r_Δ may be written in terms of the critical density of the Universe,

$$\rho_{\text{crit}}(z_f) = \frac{3H(z_f)^2}{8\pi G}, \quad (9)$$

where z_f is the cluster-formation redshift, assumed equal to the observed redshift, such that

$$M_\Delta = \frac{4}{3} \pi r_\Delta^3 \rho_{\text{crit}} \Delta, \quad (10)$$

where Δ is the density contrast. The Hubble parameter, $H(z) = 100 h E(z) \text{ km s}^{-1} \text{ Mpc}^{-1}$, is derived from the Friedmann equation. In a flat Universe $E(z)^2 = \Omega_m(1+z)^3 + \Omega_\Lambda$.

The concentration, c_Δ , is defined such that $c_\Delta = r_\Delta/r_s$. Using this definition, the normalization of the density profiles, ρ_0 , may be written as the product of the critical density and a dimensionless parameter, δ_c . Substituting $x_\Delta = r_\Delta/r_s = c_\Delta$ into the mass formulae above (equations 7 and 8) at $r = r_\Delta$ and setting them equal to equation (10) yields the following expressions for δ_c

$$\delta_c = \begin{cases} \frac{\Delta}{3} \frac{c_\Delta^3}{\ln(1+c_\Delta) - c_\Delta/(1+c_\Delta)} & \text{for NFW} \\ \frac{\Delta}{2} \frac{c_\Delta^3}{\ln(1+c_\Delta^{3/2})} & \text{for M99} \\ \frac{\Delta}{3} \frac{c_\Delta^{\alpha_3}}{{}_2F_1 \left(\alpha_3/\gamma, (\beta-\alpha)/\gamma; (\alpha_3+\gamma)/\gamma; -c_\Delta^\gamma \right)} & \text{for } M_2F_1. \end{cases} \quad (11)$$

6.2 Definition of the virial radius

The virial radius separates the region where the cluster is in hydrostatic equilibrium from where matter is still infalling. For

$\Omega_m + \Omega_\Lambda = 1$, $r_\Delta = r_{\text{vir}}$ if $\Delta = \Delta_{\text{vir}} = 178\Omega_m^{0.45}$ (Lacey & Cole 1993; Eke, Cole & Frenk 1996; Eke, Navarro & Frenk 1998). For $\Omega_m = 0.3$, $\Delta_{\text{vir}} = 104$. In an Einstein-de Sitter Universe, $\Omega_m = 1.0$ and $\Delta_{\text{vir}} = 178$. A density contrast of $\Delta = 200$ (or $\Delta = 178$) is still often used in the literature and r_{vir} and r_{200} (or r_{178}) written interchangeably. For purposes of comparison with other work in the literature, we adopt $\Delta = 200$.

7 MODELLING THE OBSERVED MASS PROFILES

CDM simulations make two robust predictions concerning the distribution of mass in dark matter haloes: the shape of the mass profile differs strongly from a power law, and the power-law slope of the inner density profile lies in the range $1.0 \lesssim \alpha \lesssim 1.5$ (see, e.g. Navarro et al. 2004). These properties are investigated for the observed mass profiles below.

7.1 General shape of the mass profile

The mass profiles in Fig. 2 are fit with the generalized mass model in equation (8), with β fixed at 3.0 and γ fixed at 1.0. Fig. 4 shows the variation in concentration parameter, scale radius, virial radius (r_{200}) and chi-square with inner slope as α is stepped through values between 0.0 and 2.0 and the fit is minimized with respect to c and r_s . (Note that the scale radius and concentration are highly negatively correlated.) The virial radius is computed by substituting $c_\Delta = r_\Delta/r_s$ into equation (11).

If the best-fitting concentration is less than 1.0 for a particular value of α , then the mass model does not agree with CDM predictions i.e. the characteristic radius, r_s , at which the profile ‘turns-over’ is greater than the virial radius. In Table 3, we show the best-fitting parameters for the M_2F_1 and power-law ($M_{\text{pow}} \propto r^{3-\alpha}$) models. When the best-fitting concentration for the M_2F_1 model is $c \ll 1.0$, the model tends to a power law. We refer to the best-fitting model as a power law when the best-fitting concentration is less than 1.0. Although not strictly true, the description serves as a useful distinction between profiles which are consistent ($c > 1$) and those which are inconsistent ($c < 1$) with the CDM model predictions.

With α a free parameter in the fits, the concentration is consistent with both $c > 1$ and $c < 1$ within the 1σ uncertainties for half the objects analysed (Abell 3112, RXJ 1347.5–1145, Abell 1795, Abell 3581, RXJ 1532.9+3021 and MS 2137.3–2353; see shaded regions in Fig. 4). In four clusters (2A 0335+096, Abell 478, PKS 0745–191 and Sersic 159–03), the best-fitting concentration is greater than 1.0 at the 68 per cent confidence level; although the best-fitting inner slope in these objects is shallower than predicted by the CDM simulations. Abell 1835 and Abell 2029 are the only two objects for which a power law is ruled out at the 1σ level and the inner slope is consistent with the CDM model.

7.2 Inner-slope measurements

The best-fitting inner slope and 1σ uncertainties are plotted for each object in Fig. 5. Also shown are the 3σ upper limits on the slope. Clusters with a best-fitting concentration less than 1.0 are indicated. It is clear from the plot that eight out of the 12 clusters analysed are consistent with the CDM model. Furthermore, the points appear to scatter around $\alpha = 1.0$, rather than $\alpha = 1.5$. An inner logarithmic slope of $\alpha = 2$ is ruled out at the 3σ level in all objects except Abell 3581; the mass profiles would therefore seem to rule out the single isothermal sphere (SIS) model which has been widely used in

the literature (e.g. Binney & Tremaine 1987). We note that there is no obvious correlation between the cluster mass and the best-fitting inner slope, although the uncertainties are too large to justify any correlation tests on the data.

The four clusters which are inconsistent with an inner slope of 1.0 at the 1σ level are 2A 0335+096, Abell 478, PKS 0745–191 and Sersic 159–03, with Abell 478, Sersic 159–03 and PKS 0745–191 consistent with $\alpha = 1.0$ at the 2σ level. Only 2A 0335+096 disagrees with the CDM predictions with 99.7 per cent confidence. We note that this is also the object for which the spectral model used provides the poorest fit (see Section 3.5) and, as discussed below, the temperature distribution in the centre is highly asymmetric between the northern and southern sectors of the cluster. The presence of an asymmetric temperature distribution in 2A 0335+096 has been shown previously by Mazzotta, Edge & Markevitch (2003).

In a recent study, Katayama & Hayashida (2004) find that six out of the 20 clusters in their sample (including Abell 478, PKS 0745–191 and 2A 0335+096) have a slope lower than unity at the 90 per cent confidence level. The authors interpret this result as being in agreement with the ‘flat core problem’ found in observations of low-mass objects.

The method used for computing the mass profiles relies on the assumptions of hydrostatic equilibrium and spherical symmetry. Whether or not the former condition is met is difficult to ascertain. Katayama & Hayashida (2004) touched on this problem by highlighting objects which exhibit obvious structure in their cores, suggesting that this may indicate a break from hydrostatic equilibrium, as well as the possibility of affecting the ambient temperature and density profile measurements. They concluded that some objects have flat inner slopes (Abell 478, PKS 0745–191 and ZW 3146), even when those with central structure (2A 0335+096 and Abell 2597) are removed.

In Fig. 5, we plot the best-fitting inner density slopes when the inner ~ 30 kpc is removed from the fits to 2A 0335+096, Abell 478, PKS 0745–191 and Sersic 159–03. It is clear that it is the innermost data point in each of these clusters which is forcing the best fit to be flat. The question is ‘how far can we trust data from the central 30 kpc?’. The challenge will be to determine the extent of any non-thermal pressure support in the central regions of these objects.

7.3 Symmetry of the temperature distribution

One clue that the gas is disturbed and not in hydrostatic equilibrium may be suggested by asymmetries in the temperature distribution. Here, we investigate whether there is any correlation between the degree of symmetry in the temperature distribution and the inner slope of the mass profile.

Fig. 6 shows the temperature distributions obtained for each of the clusters showing a flat inner density profile, together with two clusters which are consistent with the CDM mass model.

The temperature distribution of 2A 0335+096 is clearly asymmetric within the central ~ 50 kpc. This is unsurprising given that Mazzotta et al. (2003) have shown the central region contains many blobs of gas at different projected temperatures. The asymmetry does not, therefore, necessarily mean that the gas is not in hydrostatic equilibrium, but does suggest that the temperature distribution obtained from the spectral analysis may not be that of the ambient gas. In this case, the central mass measurements obtained may be incorrect. We note that Mazzotta et al. (2003) found a significant asymmetry in the temperature distribution at radii > 100 kpc. We also find that the southern half of the cluster is hotter than the

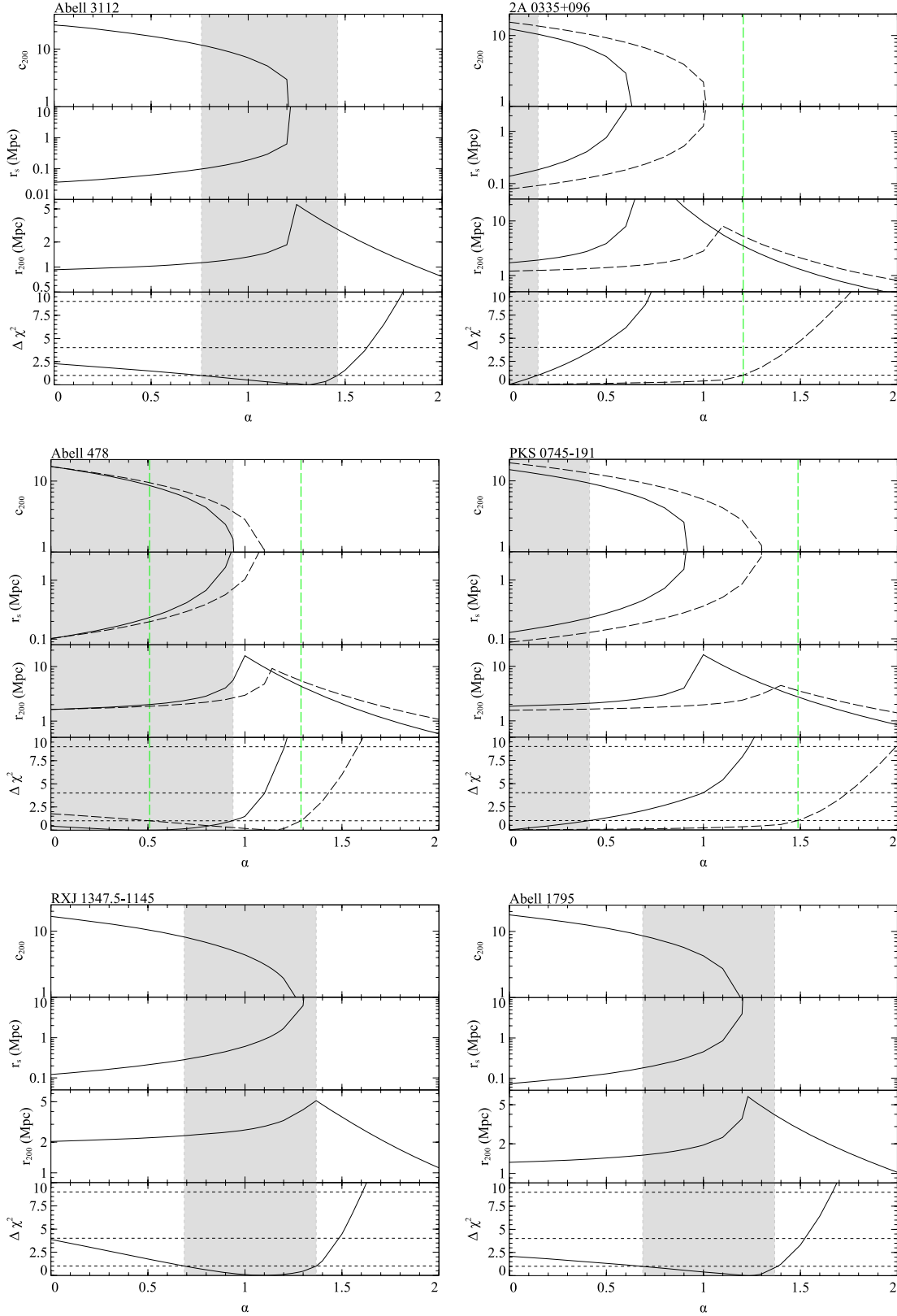


Figure 4. Plots showing variation in concentration, scale radius, virial radius and $\Delta\chi^2$ ($=\chi^2 - \chi^2_{\min}$, where χ^2_{\min} is the minimum chi-square) for values of the inner slope α between 0 and 2. The dotted horizontal lines in the bottom panel show the 1σ (68.3 per cent), 2σ (95.4 per cent) and 3σ (99.7 per cent) confidence levels for alpha. The grey-shaded regions show the parameter values which lie within the 1σ confidence interval. Note that when the concentration drops below 1.0, the scale radius is larger than the virial radius and the profile tends to a power law. Fit parameters determined with the inner 30 kpc excluded are shown with dashed lines, and the 1σ confidence limits shown by green dashed lines. (If only one green dashed line is shown then the lower limit on alpha is less than zero.)

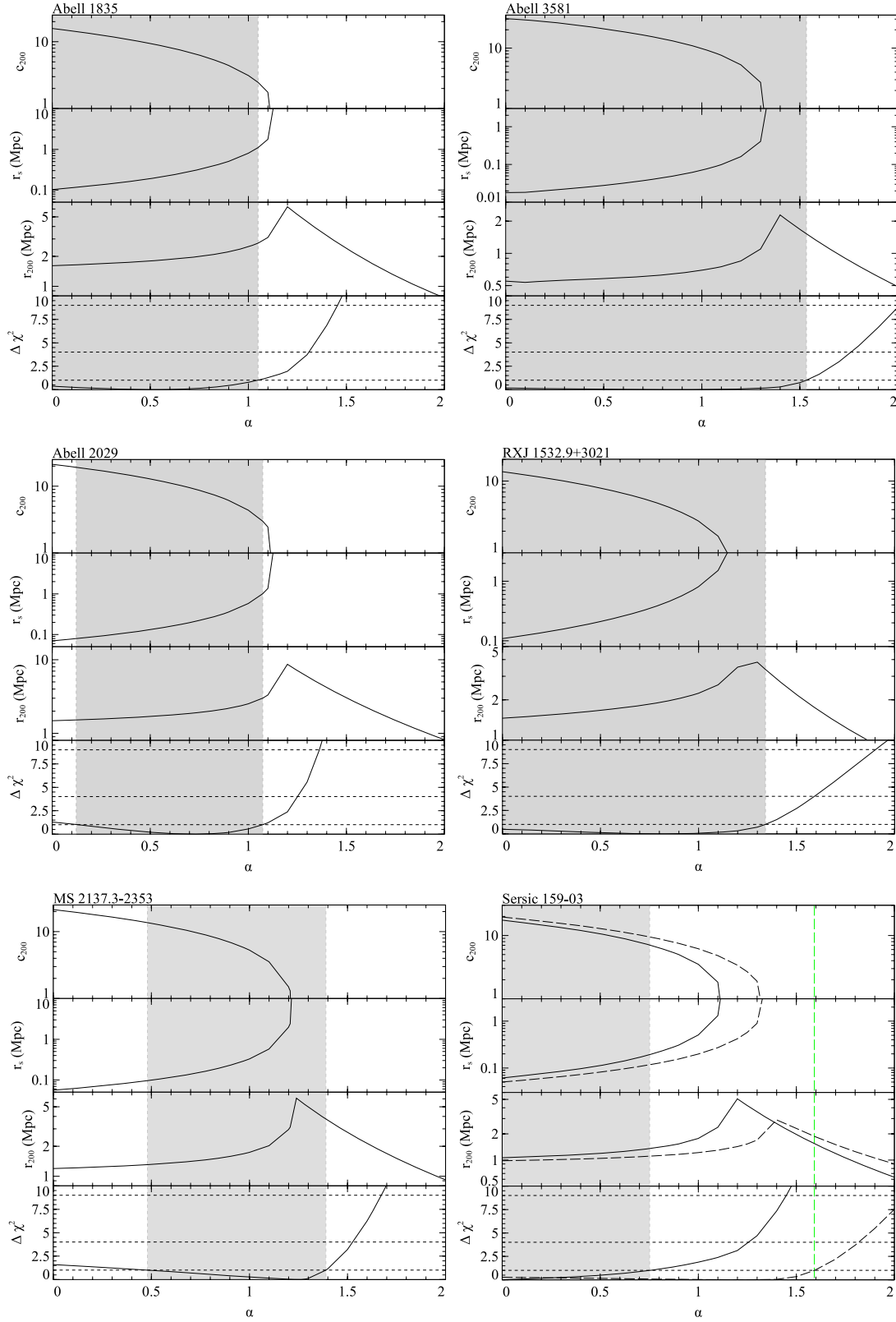


Figure 4 – Continued

northern half in the outer region, but the effect is not so pronounced. There are several differences between the analysis carried out here and the one by Mazzotta et al. (2003) which may give rise to a discrepancy in the measured temperature distributions. First,

Mazzotta et al. (2003) extracted spectra in elliptical rather than circular annuli and were therefore probing different regions of the cluster. If the temperature distribution is not symmetrical then this may lead to significant differences in the temperatures measured.

Table 3. Best-fitting slope α and corresponding chi-square for the $M_2 F_1$ and power-law models. The second row for 2A 0335+096, Abell 478, PKS 0745–191 and Sersic 159–03 shows the best fit with the inner 30 kpc excluded. The best-fitting concentration, scale radius and virial radius are shown for the $M_2 F_1$ model. The concentration and scale radius are not shown for clusters where the best fit tends to a power law (i.e. $c \ll 1.0$).

Cluster	$M_2 F_1$ model					Power-law model	
	α	c_{200}	r_s (Mpc)	r_{200} (Mpc)	χ^2 (d.o.f.)	α	χ^2 (d.o.f.)
Abell 3112	$1.31^{+0.15}_{-0.55}$	—	—	4.6	0.8 (3)	$1.31^{+0.15}_{-0.16}$	0.8 (4)
2A 0335+096	$0.00^{+0.15}_{-0.00}$	12	0.14	1.7	6.5 (2)	$0.55^{+0.09}_{-0.09}$	12.3 (3)
	$0.00^{+1.21}_{-0.00}$	15	0.08	1.2	2.3 (1)	$1.05^{+0.21}_{-0.19}$	0.7 (2)
Abell 478	$0.49^{+0.45}_{-0.49}$	9.0	0.22	2.0	6.7 (5)	$0.94^{+0.10}_{-0.10}$	7.8 (6)
	$1.14^{+0.15}_{-0.63}$	—	—	9.2	5.4 (4)	$1.14^{+0.15}_{-0.16}$	5.4 (5)
PKS 0745—191	$0.00^{+0.41}_{-0.00}$	14	0.13	1.8	2.5 (2)	$0.91^{+0.15}_{-0.16}$	6.1 (3)
	$0.00^{+1.49}_{-0.00}$	18	0.09	1.6	0.4 (1)	$1.32^{+0.22}_{-0.22}$	0.9 (2)
RXJ 1347.5—1145	$1.10^{+0.27}_{-0.41}$	3.2	0.90	2.9	3.0 (1)	$1.30^{+0.10}_{-0.10}$	3.4 (2)
Abell 1795	$1.24^{+0.15}_{-0.56}$	—	—	5.8	2.6 (2)	$1.24^{+0.15}_{-0.16}$	2.6 (3)
Abell 1835	$0.52^{+0.53}_{-0.52}$	9.2	0.20	1.8	5.9 (3)	$1.14^{+0.11}_{-0.11}$	7.5 (4)
Abell 3581	$0.88^{+0.65}_{-0.88}$	12	0.05	0.7	1.3 (3)	$1.34^{+0.22}_{-0.24}$	1.5 (4)
Abell 2029	$0.74^{+0.34}_{-0.61}$	8.9	0.21	1.9	2.4 (4)	$1.13^{+0.09}_{-0.09}$	4.1 (5)
RXJ 1532.9+3021	$0.85^{+0.49}_{-0.85}$	4.3	0.46	2.0	1.2 (2)	$1.18^{+0.20}_{-0.19}$	1.6 (3)
MS 2137.3—2352	$1.25^{+0.14}_{-0.77}$	—	—	5.9	0.2 (1)	$1.25^{+0.14}_{-0.15}$	0.2 (2)
Sersic 159—03	$0.00^{+0.75}_{-0.00}$	17	0.06	1.1	3.4 (3)	$1.09^{+0.14}_{-0.15}$	6.0 (4)
	$1.20^{+0.39}_{-1.20}$	3.4	0.42	1.4	2.5 (2)	$1.38^{+0.21}_{-0.21}$	2.5 (3)

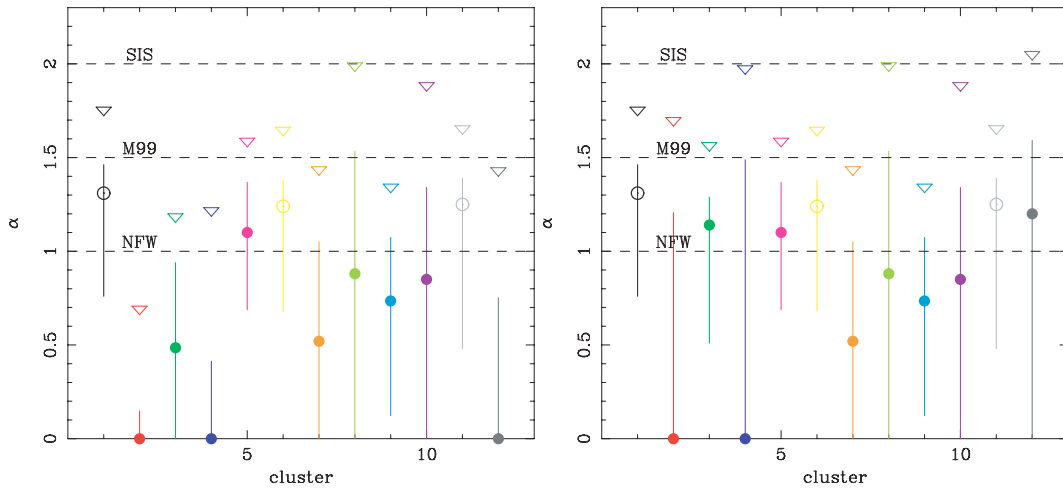


Figure 5. Left-hand panel: best-fitting inner slope. Right: best-fitting inner slope with inner 30 kpc removed in 2A 0335+096, Abell 478, PKS 0745–191 and Sersic 159–03. The error bars show the 1σ uncertainties and the downward arrows the 3σ upper limits. An open circle is used to indicate clusters with a best-fitting concentration less than 1.0. The clusters are plotted from left to right in each panel in the same order as they are listed (from top to bottom) in Table 1.

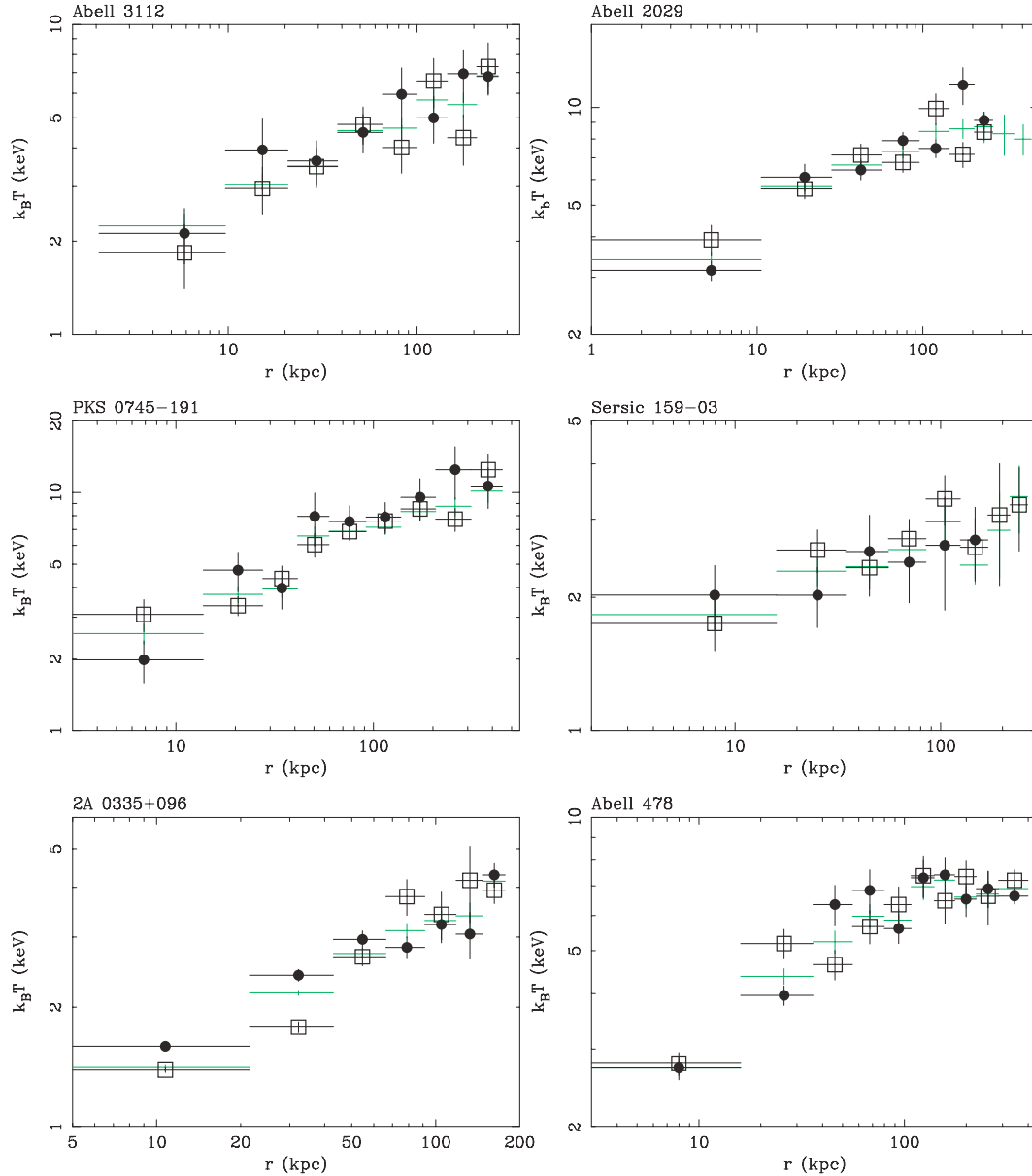


Figure 6. Plots showing the temperature distribution extracted from the northern (filled circles) and southern (open squares) sectors of the cluster. Also shown is the temperature obtained from the whole annulus at each radius (green).

In addition, Mazzotta et al. (2003) plotted the projected temperatures and allowed the absorption column density to vary between shells.

For the rest of the sample, there is little evidence for a correlation between the inner slope and the degree of symmetry in the temperature distribution.

7.4 Observed gas mass fraction profiles

The gas mass fraction profiles are shown in Fig. 2. The profiles were calculated using the relation $f_{\text{gas}}(<r) = M_{\text{gas}}(<r)/M_{\text{tot}}(<r)$, where M_{tot} is the total model-independent mass. The profiles are plotted for the whole sample in Fig. 7, with the x -axis scaled by $r_{2 \times 10^4}$ (see Section 7.5). The profiles show a variety of behaviour within $r \sim 0.02r_{\text{vir}}$, with an apparent flattening at $f_{\text{gas}} \sim 0.1$ outside this region, similar to the results of Allen et al. (2004).

7.4.1 Inner region

A high value of f_{gas} , relative to the values outside $r \sim 0.02r_{\text{vir}}$, is seen in the central bin of 2A 0335+096, Abell 478, PKS 0745-191 and Seric 159-03. These are the only objects in the sample for which the best-fitting inner slope, α , to the mass profile is inconsistent with 1.0 (see Fig. 5), suggesting a link between a high *measured* central gas mass fraction and an *apparently* shallow inner-mass density profile. The central rise in f_{gas} is clearly seen in Fig. 8, where we plot scaled gas mass fraction profiles for the three clusters where the f_{gas} peak is most obvious (2A 0335+096, Abell 478 and PKS 0745-191), together with two low-redshift clusters (Abell 3112 and Abell 1795), whose best-fitting mass profiles are consistent with $\alpha = 1.0$, for comparison. The latter two objects show an increase in f_{gas} from the centre outwards, as expected from the CDM simulations

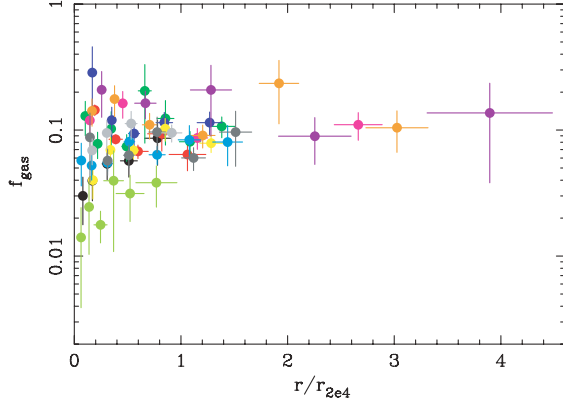


Figure 7. Gas mass fraction profiles for the sample with the x -axis scaled by $r_{2 \times 10^4}$ (see Table 4). The colour-coding is the same as used in Fig. 5.

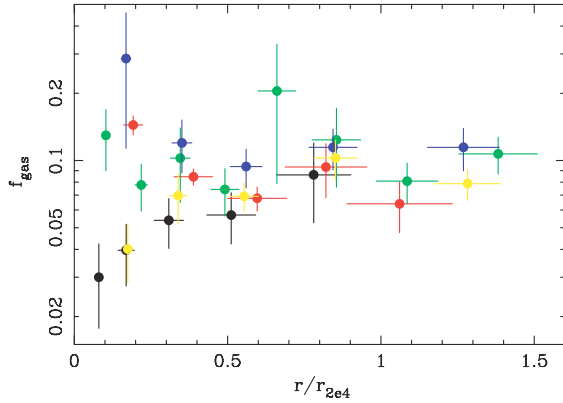


Figure 8. Gas mass fraction profiles for Abell 3112 (black), 2A 0335+096 (red), Abell 478 (green), PKS 0745-191 (blue) and Abell 1795 (yellow).

(Eke et al. 1998). With the exception of Abell 3581, whose profile drops towards the centre, the remaining objects in the sample have relatively flat f_{gas} profiles in the inner region.

Katayama & Hayashida (2004) found a negative correlation between α and the value of f_{gas} near the centre of the cluster. They interpret this as a tendency for clusters with gas-rich cores to have flat central density profiles. It seems just as likely that the high gas mass fraction measured in the central parts of these objects results from an underestimation of the total mass,⁵ supporting the presence of non-thermal pressure in the core or suggesting incorrect spectral modelling of the data (note that the spectral fit to the emission from the centre of 2A 0335+096 is poor).

7.5 NFW model fits

The majority of the clusters in the sample are consistent with the NFW mass model, that is, $\alpha = 1.0$ (see Fig. 5). Here, we find the best-fitting scale radius and concentration for each cluster assuming an NFW profile. (For clusters where the NFW model is excluded at the 1σ level, we remove the inner 30 kpc from the fit). It is important to stress that attempting to measure r_s is pushing the data to its limits since the best-fitting scale radius in general lies beyond the radius

⁵ If the true gas mass fraction profiles of the objects studied here with best-fitting $\alpha < 1.0$ are either flat or drop into the centre then this implies that the total mass in the inner region has been underestimated by at least a factor of 2. The total mass profiles would then be consistent with $\alpha \sim 1.0$.

at which mass measurements can be made (see Fig. 2). The values obtained for r_s are therefore strongly dependent on the outermost data point in the mass profile. It also makes the value difficult to constrain and, while some of the clusters show evidence for a turn-over in the mass profile, more precise determination of the scale radius would require mass measurements out to a larger fraction of the virial radius.

We compute the concentration at three overdensities: $\Delta = 2 \times 10^4$, 2500 and 200. For $\Delta = 2 \times 10^4$, the value obtained for r_Δ is independent of the accuracy of r_s since in each case r_Δ lies within the radius at which mass measurements have been obtained. However, for $\Delta = 200$ the value obtained for r_{200} is highly dependent on the accuracy of r_s (since it involves extrapolating the NFW model using r_s). The values for r_{200} are shown for interest, but are not used for any subsequent analysis. The concentration is also computed at $\Delta = 2500$. This allows comparison of our results for PKS 0745-191, Abell 1835, RXJ 1347.5-1145 and MS 2137.3-2352 with those found by Allen, Schmidt & Fabian (2001). (Note that for the more massive clusters r_{2500} lies within the radius at which mass measurements have been obtained.) The data used here for PKS 0745-191, Abell 1835 and RXJ 1347.5-1145 are the same data used by Allen et al. (2001). The values of r_{2500} are consistent between the two studies within the 1σ uncertainties. However, Allen et al. (2001) generally find a higher concentration (and therefore lower scale radius) than the results found here. The difference in values is not surprising given the discussion above concerning the difficulty of measuring r_s .

The best-fitting parameters are shown in Table 4. The mass enclosed within a density contrast of 2×10^4 is computed using equation (10). The cluster mass profiles, with the x -axis scaled by r_Δ , are shown in Fig. 9. The y -axis for each mass profile is scaled by $M_{\text{crit}} = (4/3)\pi r_\Delta^3 \rho_{\text{crit}} \Delta$. Each mass profile should therefore coincide if the concentration varies little from halo to halo.⁶

N -body simulations predict a weak dependence of halo concentration on mass, with $c_{\text{vir}} \propto M_{\text{vir}}^{-\alpha}$ and $\alpha \sim 0.1$ for all haloes at a given redshift. In Fig. 10, we plot $c_{2 \times 10^4}$ against $M_{2 \times 10^4}$. (Note that we do not plot c_{200} against M_{200} here since the calculation of M_{200} depends on r_{200} which is itself an uncertain number.) The concentration is scaled to a redshift of zero using the concentration-redshift dependence found in the N -body simulations by Bullock et al. (2001). The relation predicts that for haloes of the same mass, the concentration is proportional to $(1+z)^{-1}$. We show the best-fitting power-law model to the data along with the theoretical prediction of Bullock et al. (2001).⁷ The theoretical model is applicable out to halo masses of $M_{\text{vir}} \lesssim 10^{16} M_\odot$, giving rise to a cut-off in the predicted $c_{2 \times 10^4} - M_{2 \times 10^4}$ relation at $M_{2 \times 10^4} \sim 10^{14} M_\odot$. The best-fitting power-law index is $\alpha \sim 0.2$. The data appear to agree well with the theoretical model of Bullock et al. (2001).

8 SUMMARY

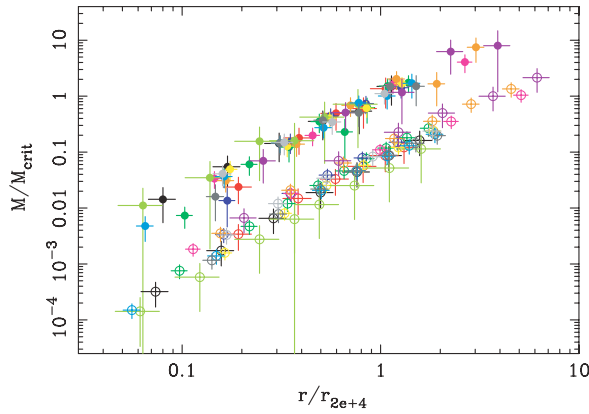
The shape of the mass distribution in virialized haloes provides a sensitive test of the CDM paradigm. In this paper, we have analysed

⁶ Substituting $r' = r/r_\Delta$ into equation (7) gives $M(r')/M_{\text{crit}} = [\ln(1 + c_\Delta r') - c_\Delta r'/(1 + c_\Delta r')]/[\ln(1 + c_\Delta) - c_\Delta/(1 + c_\Delta)]$.

⁷ The model data are found using the FORTRAN codes provided on J. Bullock's webpage. The theoretical $c_{\text{vir}} - M_{\text{vir}}$ relation is scaled to $c_{2 \times 10^4} - M_{2 \times 10^4}$ using the definition $M_{2 \times 10^4} = M_{\text{vir}} \times f(c_{2 \times 10^4})/f(c_{\text{vir}})$, where $f(c) = \ln(1+c) - c/(1+c)$, $c_{2 \times 10^4} = c_{\text{vir}} \times (\Delta_{\text{vir}} M_{2 \times 10^4} / \Delta_{2 \times 10^4} M_{\Delta_{\text{vir}}})^{1/3}$ and $\Delta_{\text{vir}} = 104$.

Table 4. Best-fitting NFW model parameters for $\Delta = 200$ and 2×10^4 . Also shown are the scaled radii enclosing a density contrast of $\Delta = 2500$.

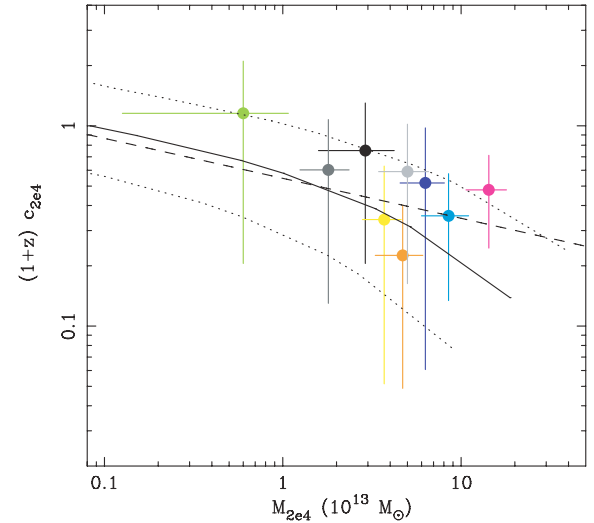
Cluster	r_s (Mpc)	c_{200}	r_{200} (Mpc)	$c_{2 \times 10^4}$	$r_{2 \times 10^4}$ (Mpc)	$M_{2 \times 10^4}$ ($10^{13} M_\odot$)	r_{2500} (Mpc)	χ^2 (d.o.f.)
Abell 3112	$0.19^{+0.39}_{-0.09}$	$7.06^{+3.62}_{-3.23}$	$1.32^{+0.88}_{-0.35}$	$0.70^{+0.57}_{-0.44}$	$0.13^{+0.02}_{-0.02}$	$2.9^{+1.5}_{-1.1}$	$0.42^{+0.19}_{-0.09}$	1.3 (4)
2A 0335+096	$0.13^{+5.38}_{-0.10}$	$8.18^{+18.83}_{-7.20}$	$1.05^{+4.42}_{-0.39}$	$0.88^{+3.22}_{-0.85}$	$0.11^{+0.02}_{-0.01}$	$1.7^{+1.0}_{-0.5}$	$0.34^{+0.56}_{-0.10}$	1.7 (1)
Abell 478	$1.03^{+\infty}_{-0.63}$	$2.88^{+2.02}_{-2.88}$	$2.97^{+14.8}_{-1.02}$	$0.16^{+0.24}_{-0.16}$	$0.16^{+0.02}_{-0.01}$	$5.7^{+1.7}_{-1.5}$	$0.76^{+0.67}_{-0.19}$	5.6 (5)
PKS 0745–191	$0.36^{+0.98}_{-0.20}$	$5.46^{+3.22}_{-2.88}$	$1.96^{+1.51}_{-0.50}$	$0.47^{+0.48}_{-0.34}$	$0.17^{+0.02}_{-0.01}$	$6.3^{+1.9}_{-1.6}$	$0.59^{+0.27}_{-0.11}$	0.6 (2)
RXJ 1347.5–1145	$0.60^{+0.46}_{-0.22}$	$4.37^{+1.39}_{-1.24}$	$2.64^{+0.70}_{-0.48}$	$0.33^{+0.18}_{-0.14}$	$0.20^{+0.02}_{-0.02}$	$14.3^{+3.6}_{-3.7}$	$0.76^{+0.13}_{-0.10}$	3.0 (2)
Abell 1795	$0.45^{+1.59}_{-0.23}$	$4.28^{+2.23}_{-2.41}$	$1.94^{+1.86}_{-0.51}$	$0.32^{+0.30}_{-0.24}$	$0.14^{+0.01}_{-0.01}$	$3.7^{+1.0}_{-0.8}$	$0.55^{+0.28}_{-0.11}$	3.0 (3)
Abell 1835	$0.80^{+1.59}_{-0.38}$	$3.13^{+1.37}_{-1.44}$	$2.50^{+1.55}_{-0.64}$	$0.18^{+0.16}_{-0.12}$	$0.15^{+0.01}_{-0.01}$	$4.7^{+1.4}_{-1.4}$	$0.65^{+0.20}_{-0.12}$	6.6 (4)
Abell 3581	$0.07^{+0.23}_{-0.04}$	$9.81^{+6.30}_{-5.40}$	$0.69^{+0.65}_{-0.20}$	$1.13^{+1.05}_{-0.79}$	$0.08^{+0.02}_{-0.01}$	$0.6^{+0.6}_{-0.3}$	$0.23^{+0.16}_{-0.06}$	1.3 (4)
Abell 2029	$0.58^{+0.94}_{-0.25}$	$4.38^{+1.64}_{-1.76}$	$2.52^{+1.45}_{-0.59}$	$0.33^{+0.22}_{-0.19}$	$0.19^{+0.02}_{-0.02}$	$8.5^{+2.7}_{-2.3}$	$0.72^{+0.26}_{-0.13}$	2.9 (5)
RXJ 1532.9+3021	$0.81^{+13.07}_{-0.53}$	$2.77^{+2.28}_{-2.28}$	$2.24^{+4.72}_{-0.85}$	$0.15^{+0.27}_{-0.14}$	$0.12^{+0.02}_{-0.02}$	$2.9^{+1.3}_{-1.3}$	$0.56^{+0.31}_{-0.15}$	1.3 (3)
MS 2137.3–2353	$0.34^{+0.74}_{-0.16}$	$5.28^{+2.41}_{-2.52}$	$1.74^{+1.22}_{-0.42}$	$0.45^{+0.35}_{-0.30}$	$0.15^{+0.02}_{-0.01}$	$5.0^{+1.7}_{-1.4}$	$0.52^{+0.22}_{-0.10}$	0.4 (2)
Sersic 159–03	$0.20^{+0.37}_{-0.10}$	$6.16^{+3.42}_{-2.79}$	$1.22^{+0.70}_{-0.30}$	$0.57^{+0.52}_{-0.36}$	$0.11^{+0.01}_{-0.01}$	$1.8^{+0.6}_{-0.5}$	$0.38^{+0.14}_{-0.07}$	2.5 (3)

**Figure 9.** Scaled mass profiles: total (filled circles) and gas (open circles) mass profiles. The colour-coding is the same as used in Fig. 5.

the mass profiles of a sample of galaxy clusters. The main results are as follows.

(i) The mass distribution in the majority of the objects studied are consistent with the NFW model (Navarro et al. 1995). Four objects in the sample (2A 0335+096, Abell 478, PKS 0745–191 and Sersic 159–03) exhibit a flatter core.

(ii) The gas mass fraction measured in the central region of the clusters with flat core density profiles is high, indicating that the total mass may be underestimated within the central ~ 30 kpc of these objects. If this is the case, then either a significant non-thermal pressure component exists in the core or the X-ray emission has been incorrectly modelled. For 2A 0335+096 the central temperature distribution is asymmetric, suggesting that the temperature and density

**Figure 10.** Plot showing the dependence of concentration on halo mass. The theoretical mass–concentration relation predicted by Bullock et al. (2001) (solid curve) and 1σ confidence limits (dotted curves). Also shown is the best-fitting power-law model to the data (dashed line). The colour-coding is the same as used in Fig. 5.

obtained may not accurately represent the ambient gas properties in the core for this object.

(iii) CDM simulations predict that the mass distribution in virialized haloes differs from a power law, turning-over at a characteristic radius, $r_s = r_{\text{vir}}/c$. With α a free parameter in the fits, a power-law density profile is ruled out at the 1σ level in Abell 1835 and Abell 2029. (A power law is also ruled out at the 1σ level in

2A 0335+096, Abell 478, PKS 0745–191 and Sersic 159–03, although the inner slope in these objects is inconsistent with the CDM predictions). Otherwise, we find no strong evidence for the expected turn-over in the mass profile. For three objects in the sample (Abell 3112, Abell 1795 and MS 2137.3–2353), the best-fitting model is a power law.

(iv) The mass–concentration relation at a density contrast of 2×10^4 is consistent with the theoretical prediction from N -body simulations by Bullock et al. (2001).

9 DISCUSSION

In the CDM scenario, simulations predict a universal form for the distribution of dark matter in virialized haloes, independent of both mass and cosmological parameters (Navarro et al. 1995, 1996, 1997). The universal density profile has a cuspy core, $\rho \propto r^{-\alpha}$, rolling over to $\rho \propto r^{-3}$ at a characteristic radius known as the scale radius. The majority of the mass profiles obtained for the cluster sample in this paper are consistent with the NFW model; only four objects exhibit shallower density cores (2A 0335+096, Abell 478, PKS 0745–191 and Sersic 159–03). The discrepancy between the mass distribution measured in these systems and the NFW profile need not indicate any problem with the CDM paradigm, but may instead result from an underestimation of the core mass. The high gas mass fraction measured in the central region of all four systems with flat inner density profiles certainly suggests that this may be the case. Spurious low mass measurements could be caused by the presence of non-thermal pressure support in the inner regions of these objects and/or incorrect spectral modelling of the emission from clusters with significant core substructure. Another possibility concerns the importance of non-spherical effects on the measured mass distribution. Hayashi et al. (2004) have recently shown that rotation curves obtained from galaxies with triaxial haloes may, in some cases, infer an erroneously flat core to the mass profile if spherical symmetry is assumed. The effects of non-axial symmetry on X-ray measurements of cluster masses have been investigated by Piffaretti, Jetzer & Schindler (2003). The authors show that the core mass will be underestimated if the halo is compressed along the line of sight. It is interesting that both Abell 478 and PKS 0745–191 both appear highly elliptical. Analytic solutions to the hydrostatic equation for gas residing in a triaxial dark matter potential have been computed for isothermal and polytropic temperature distributions by Lee & Suto (2003). These formula may in future work be applied to clusters to compute the mass distribution.

Determining whether or not the flat cores measured in some clusters are real is of great importance to cosmological and cluster studies; if they *are* real, then either our understanding of dark matter is incorrect, or non-gravitational processes, such as dynamical friction acting on cluster galaxies moving through the core (El-Zant et al. 2004), modify the mass distribution.

The work carried out here has put some constraints on the mass distribution in a sample of galaxy clusters. Tighter constraints will be possible by imaging the clusters out to larger radii or, for the case of high-redshift objects, by taking longer exposures, so that the radius at which the profile ‘turns-over’ may be robustly detected.

In future work, it will be important to investigate effects which might reconcile the observed flat density profiles found in this study with the CDM model predictions. One possible cause for the discrepancy is non-thermal pressure support in the core. Sanders, Fabian & Dunn (2005) found inverse Compton emission from relativistic electrons which can contribute significant pressure near the centre

of the Perseus cluster. Careful comparison of X-ray and lensing masses will also be important.

ACKNOWLEDGMENTS

LMV is grateful to Roderick Johnstone and Steve Allen for their help and advice. We thank the referee for several comments which led to a significantly improved manuscript. ACF and LMV acknowledge support from The Royal Society and PPARC, respectively.

REFERENCES

- Allen S. W., 1998, MNRAS, 296, 392
- Allen S. W., Schmidt R. W., Fabian A. C., 2001, MNRAS, 328, L37
- Allen S. W., Schmidt R. W., Ebeling H., Fabian A. C., van Speybroeck L., 2004, MNRAS, 353, 457
- Anders E., Grevesse N., 1989, GeCoA, 53, 197
- Arabadjis J. S., Bautz M. W., Arabadjis G., 2004, ApJ, 617, 303
- Arnaud K. A., 1996, in Jacoby G. H., Barnes J., eds, ASP Conf. Ser. Vol. 101, Astronomical Data Analysis Software and Systems V. Astron. Soc. Pac., San Francisco, p. 17
- Birzan L., Rafferty D. A., McNamara B. R., Wise M. W., Nulsen P. E. J., 2004, ApJ, 607, 800
- Balucinska-Church M., McCammon D., 1992, ApJ, 400, 699
- Binney J., Tremaine S., 1987, Galactic Dynamics. Princeton Univ. Press, Princeton, NJ
- Bullock J. S., Kolatt T. S., Sigad Y., Somerville R. S., Kravtsov A. V., Klypin A. A., Primack J. R., Dekel A., 2001, MNRAS, 321, 559
- Cole S., Lacey C., 1996, MNRAS, 281, 716
- Crone M. M., Evrard A. E., Richstone D. O., 1994, ApJ, 434, 402
- Dickey J. M., Lockman F. J., 1990, ARA&A, 28, 215
- Diemand J., Zemp M., Moore B., Stadel J., Carollo M., 2005, ArXiv Astrophysics e-prints
- Dubinski J., Carlberg R. G., 1991, ApJ, 378, 496
- Eke V. R., Cole S., Frenk C. S., 1996, MNRAS, 282, 263
- Eke V. R., Navarro J. F., Frenk C. S., 1998, ApJ, 503, 569
- El-Zant A. A., Hoffman Y., Primack J., Combes F., Shlosman I., 2004, ApJ, 607, L75
- Fillmore J. A., Goldreich P., 1984, ApJ, 281, 9
- Frenk C. S., White S. D. M., Davis M., Efstathiou G., 1988, ApJ, 327, 507
- Fukushige T., Makino J., 1997, ApJ, 477, L9
- Fukushige T., Makino J., 2001, ApJ, 557, 533
- Fukushige T., Makino J., 2003, ApJ, 588, 674
- Ghigna S., Moore B., Governato F., Lake G., Quinn T., Stadel J., 2000, ApJ, 544, 616
- Gunn J. E., Gott J. R. I., 1972, ApJ, 176, 1
- Hayashi E. et al., 2004, MNRAS, 355, 794
- Hayashi E. et al., 2004, ApJ, submitted (astro-ph/0408132)
- Hoffman Y., Shaham J., 1985, ApJ, 297, 16
- Jing Y. P., Suto Y., 2000, ApJ, 529, L69
- Johnstone R. M., Fabian A. C., Morris R. G., Taylor G. B., 2005, MNRAS, 356, 237
- Katayama H., Hayashida K., 2004, Adv. Space Res., 34, 2519
- Klypin A., Kravtsov A. V., Bullock J. S., Primack J. R., 2001, ApJ, 554, 903
- Kravtsov A. V., Klypin A. A., Khokhlov A. M., 1997, ApJS, 111, 73
- Lacey C., Cole S., 1993, MNRAS, 262, 627
- Lee J., Suto Y., 2003, ApJ, 585, 151
- Liedahl D. A., Osterheld A. L., Goldstein W. H., 1995, ApJ, 438, L115
- Mazzotta P., Edge A. C., Markevitch M., 2003, ApJ, 596, 190
- Mewe R., Gronenschild E. H. B. M., van den Oord G. H. J., 1985, A&AS, 62, 197
- Moore B., Quinn T., Governato F., Stadel J., Lake G., 1999, MNRAS, 310, 1147 (M99)
- Navarro J. F., Frenk C. S., White S. D. M., 1995, MNRAS, 275, 720 (NFW)
- Navarro J. F., Frenk C. S., White S. D. M., 1996, ApJ, 462, 563
- Navarro J. F., Frenk C. S., White S. D. M., 1997, ApJ, 490, 493
- Navarro J. F. et al., 2004, MNRAS, 349, 1039

Piffaretti R., Jetzer P., Schindler S., 2003, *A&A*, 398, 41
Pointecouteau E., Arnaud M., Pratt G. W., 2005, *A&A*, 435, 1
Power C., Navarro J. F., Jenkins A., Frenk C. S., White S. D. M., Springel
V., Stadel J., Quinn T., 2003, *MNRAS*, 338, 14
Sanders J. S., Fabian A. C., Dunn R. J. H., 2005, *MNRAS*, 360, 133
Syer D., White S. D. M., 1998, *MNRAS*, 293, 337
Tormen G., Bouchet F. R., White S. D. M., 1997, *MNRAS*, 286, 865

Voigt L. M., Fabian A. C., 2004, *MNRAS*, 347, 1130
Wambsganss J., Bode P., Ostriker J. P., 2005, *ApJ*, 635, L1
White S. D. M., Zaritsky D., 1992, *ApJ*, 394, 1

This paper has been typeset from a $\mathrm{T}_{\mathrm{E}}\mathrm{X}/\mathrm{L}^{\mathrm{A}}\mathrm{T}_{\mathrm{E}}\mathrm{X}$ file prepared by the author.